

<https://doi.org/10.1038/s42005-024-01706-6>

Synchronization of non-weakly coupled aeroelastic oscillators

Check for updates

Doron Shenhav Feigin & Oriel Shoshani

Synchronized oscillators are ubiquitous in nature and engineering. Despite several models that have been proposed to treat synchronized oscillators beyond weak coupling, the widely accepted paradigm holds that synchronization occurs due to weak interactions between oscillating objects, hence limiting the predictive power of such models to the weak coupling limit. Here, we report a theoretical modeling and experimental observation of a synchronized pair of non-weakly coupled aeroelastic oscillators. We find quantitative agreement between the experiments and our theoretical higher-order phase model of non-weak coupling. Our results establish that synchronization experiments can be accurately reproduced and interpreted by theoretical modeling of non-weakly coupled oscillators, extending the range of validity and prediction power of theoretical phase models beyond the weak coupling limit.

From superconductivity¹ and superfluidity² at the subatomic scale to orbital resonances of planets at celestial scales³, synchronization pervades all of nature, science, and engineering. Since Huygens' observation in 1665 of an odd kind of sympathy between a pair of pendulum clocks, researchers made immense progress in the theory, experiments, and applications of synchronization. Examples include theoretical derivation of reduced-order phase models to analyze synchronization^{4–8}, theoretical discoveries and experimental observations of exotic synchronization phenomena, such as cluster synchronization⁹, phase waves and turbulence^{10–12}, and chimera states^{13–16}, analysis of complex fluid flows^{17–20}, usage of synchronization for frequency stabilization^{21–24}, for frequency synthesizers^{25–27}, and for neuro-morphic computing^{28–30}. In this continuous effort to explore synchronization and stretch the envelope of its applications, there have been numerous successful attempts to model the synchronization of non-weakly coupled oscillators by using advanced and sophisticated phase reduction methods^{31–35}. However, the widely accepted paradigm holds that synchronization occurs due to a weak coupling (or interaction) between self-sustained oscillating objects. From this assumption of weak coupling, one can readily derive the well-known Kuramoto phase model for many globally coupled oscillators⁴ or the Adler equation³⁶, which is a special case of the Kuramoto phase model for a pair of oscillators^{6,22,23}.

This paper investigates the mutual synchronization of a pair of aeroelastic oscillators with a non-weak coupling. We show that the noisy Adler equation of weakly coupled oscillators gives an inaccurate prediction that misses the synchronization range by almost 20%. Unlike recent studies that use sophisticated phase reduction methods^{37–40}, we take a simple and straightforward approach, which can be viewed as a direct modification of the classical Haken-type phase reduction method^{41,42}, to derive a generalized phase model that accurately predicts the experimental measurements for

non-weak coupling. Our findings show that the strict requirement of weak coupling, described by the Adler equation, can be relaxed and replaced by a higher-order phase model that not only describes the synchronization of weakly coupled oscillators but also adequately applies to larger coupling strengths.

Results and discussion

Experiments

We conducted the experiments in a low-speed wind tunnel (Fig. 1) with a test section of a $0.7 \times 0.7 \text{ m}^2$ rectangular cross-section area that is 1.35 m long. The speed of the streamwise airflow in the test section can be tuned to different average values between $U_\infty = 2 - 25 \text{ m/s}$. We anchored a pair of mechanical resonators inside the test section. Each mechanical resonator is composed of a square aluminum prism [hydraulic diameter $h = 0.02 \text{ m}$, length $\ell_p = 0.56 \text{ m}$, mass $m = 0.247 \text{ kg}$] that is vertically mounted and connected to a pair of aluminum cantilevers with nominal dimensions of $1(\text{length}) \times 0.04(\text{width}) \times 0.005(\text{thickness}) \text{ m}^3$, actual adjustable length (form anchor to prism) $\ell_{1,2} = 0.56 - 0.62 \text{ m}$, a flexural rigidity $EI = 16.8 \text{ kg} \cdot \text{m}^3/\text{s}^2$, and a mass per unit length $\rho = 0.46 \text{ kg/m}$.

The self-sustained oscillations of the mechanical resonators occur due to a transverse aerodynamic force^{43,44} that serves as a feedback loop, where beyond a threshold value of airflow speed, the added linear damping from the airflow becomes negative—such that the airflow pumps energy to the resonator. Consequently, the transverse motion of the resonator increases until nonlinear effects commence and the amplitude saturates at a stable limit cycle. We use the term aeroelastic oscillator to describe the actively self-oscillating component that includes the mechanical resonator with the transverse aerodynamic force beyond the instability threshold. We note that our aeroelastic oscillator can generate multiple coexisting limit cycles at a

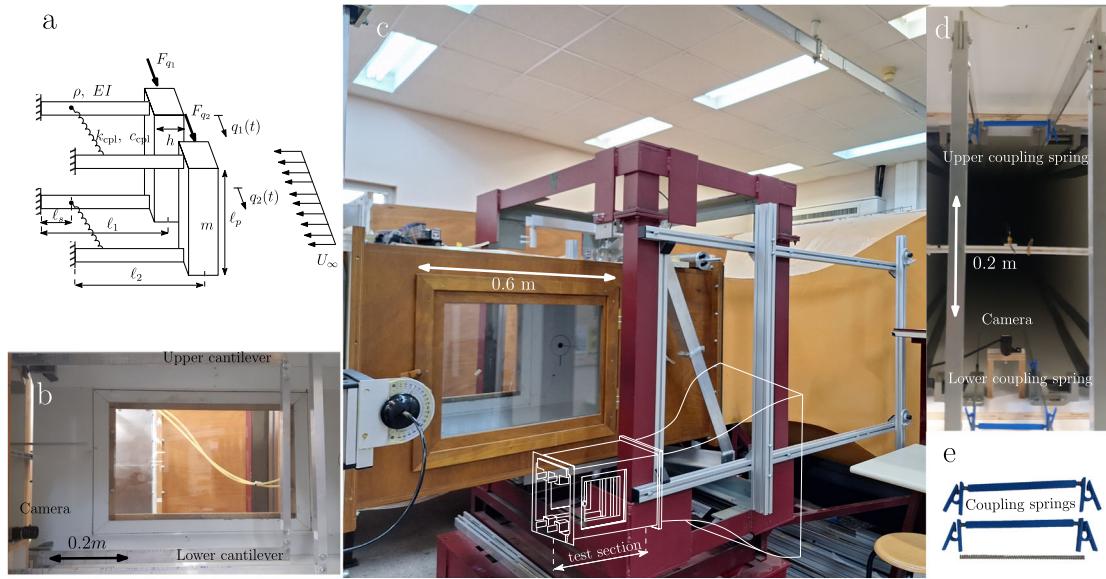


Fig. 1 | Coupled aeroelastic oscillators. **a** Each of the two identical rigid prisms (mass m , length ℓ_p , and rectangular cross-section $h \times h$) is connected to a pair of identical elastic aluminum cantilevers with a mass density per unit length ρ , flexural rigidity EI , and variable length $\ell_{1,2}$. **b** The variable length of the cantilevers $\ell_{1,2}$, enables control of the oscillation frequency of the prisms and can be adjusted (from anchor to prism) in the range of 0.56–0.62 m. The white scale bar shows a length of 20 cm. **c** The upstream speed U_∞ of the air in the streamwise direction of the test

section produces transverse forces on the prisms $F_{q_{1,2}}$ that induce self-sustained oscillations of the prisms, $q_1(t)$ and $q_2(t)$. **d** The prisms interact with each other via a pair of viscoelastic springs (c_{cpl} , k_{cpl}) that are attached to the upper and lower cantilevers. The coupling strength is adjusted by changing the springs' distance from the cantilevers' clamped end ℓ_c . **e** The coupling springs are covered by a custom-made 3D-printed smooth pipe to prevent buckling and minimize energy dissipation due to friction and anchoring losses.

certain range of airflow speed; however, in our study, we used a constant airflow speed of 8 m/s in which there is a single (and stable) limit cycle (Methods).

We imposed the coupling between the oscillators by a pair of springs that are attached to the lower and upper cantilevers (Fig. 1). Each spring moves inside a custom-made 3D-printed smooth pipe, which prevents spring buckling and minimizes energy dissipation due to friction and anchoring losses. We estimated the stiffness [$k_{cpl} = 203.250 \text{ kg/s}^2$] and damping constant [$c_{cpl} = 0.107 \text{ kg/s}$] of the viscoelastic springs from ring-down measurements (Methods), which also validate that the coupling forces are linear throughout the range of amplitudes that we consider in this paper.

We recorded the transverse motions of the prisms with a high-speed camera (IDS, UI-3140CP Rev. 2) equipped with an M1214-MP2 lens at a frame rate of 1.2 KHz, which is three orders of magnitude higher than the measured oscillation frequency [$\approx 5.55 \text{ Hz}$]. We processed the videos using an in-house MATLAB-based image processing routine to extract the position of the prisms as functions of time (Methods), and we used the built-in Hilbert transform of MATLAB to extract the phases $\phi_{1,2}(t)$ and amplitudes $a_{1,2}(t)$ of the oscillators from the time tracks of the prisms' positions.

Theory

We derived a reduced-order model for the amplitude of each oscillator $a_{1,2}$ and their phase difference $\psi = \phi_2 - \phi_1$ (see Supplementary Note 1), which takes the form

$$\dot{a}_{1,2} = -F(a_{1,2}) \pm \kappa a_{2,1} \sin \psi + \zeta_{1,2}(t), \quad (1)$$

$$\dot{\psi} = \Delta\omega + G(a_1, a_2) - \kappa \left(\frac{a_1}{a_2} - \frac{a_2}{a_1} \right) \cos \psi + \zeta_3(t), \quad (2)$$

where $F(a_{1,2}) = \sum_n f_n a_{1,2}^n$ models the amplitude dynamics of the uncoupled aeroelastic oscillator and the saturation at a stable limit-cycle $a_{1,2} = a_{ss}$, which satisfy the conditions $F(a_{ss}) = 0$ and $F'(a_{ss}) > 0$, κ is the reactive coupling strength (the dissipative coupling c_{cpl} is found to be negligible, see Methods), $\zeta_j(t)$ are delta-correlated Gaussian noises $\langle \zeta_i(t) \zeta_j(t') \rangle = 2\sigma_i^2 \delta_{ij} \delta(t - t')$ of low intensity (σ_i^2) that account for the turbulence-

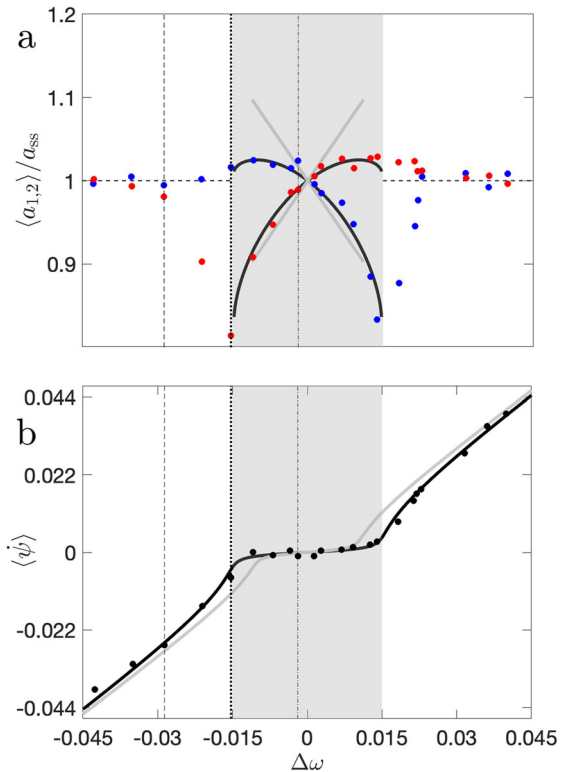


Fig. 2 | Synchronization of aeroelastic oscillators with a non-weak coupling. Comparison between experimental data (points) and theoretical predictions for the higher-order model [Eqs. (3)–(4), black curve] and the Adler equation [Eqs. (3)–(4) truncated at order $O(\kappa)$, gray curve]. The theoretical predictions for the amplitudes (a) exist only in the synchronized range (shaded region), where the current of the phase difference (b) is zero. The vertical dashed, dotted, and dashed-dotted lines correspond to the experimental data shown in the top, center, and bottom panels of Fig. 3, respectively.

induced random fluctuations, $\Delta\omega = \omega_2 - \omega_1$ is the frequency mismatch of the uncoupled aeroelastic oscillators, and $G(a_1, a_2) = \sum_n g_n(a_1^{2n} - a_2^{2n})$ encapsulates the difference in the frequency pulling of the uncoupled aeroelastic oscillators (see Supplementary Note 1).

To derive a phase model for ψ , we take a perturbative approach, where we set $a_{1,2} = a_{ss} + \sum_n \kappa^n \delta a_{1,2}^{(n)}$, assume that amplitude fluctuations are very small $\zeta_{1,2} \sim O(\kappa^3)$, and find the following expansions for the steady-state amplitudes (see Methods)

$$a_{1,2} = a_{ss} \pm \frac{\kappa a_{ss}}{F'(a_{ss})} \sin \psi - \frac{\kappa^2 a_{ss} [2F'(a_{ss}) + a_{ss} F''(a_{ss})]}{2F'^3(a_{ss})} \sin^2 \psi + O(\kappa^3), \quad (3)$$

where F' and F'' are the first and second derivatives of F with respect to the amplitude. Next, we substituted the expansions of $a_{1,2}$ into Eq. (2), and find that, to order $O(\kappa^2)$, the phase model for ψ is given by

$$\dot{\psi} = \Delta\omega - c_1 \kappa \sin \psi - c_2 \kappa^2 \sin 2\psi + \zeta_3(t), \quad (4)$$

where $c_1 = [a_{ss}/F'(a_{ss})](\partial_{a_2} G - \partial_{a_1} G)|_{a_{ss}}$, and $c_2 = [2/F'(a_{ss})]$.

Before we proceed to the Eq. (4) analysis, we make some remarks on the assumptions and validity of Eqs. (3)–(4). Strictly speaking, Eqs. (3)–(4) are valid only inside the synchronization range, where $\Delta\omega \sim O(\kappa)$, $\psi(t)$ is a slowly varying function of time [$\dot{\psi} \sim O(\kappa)$], and $a_{1,2}(t)$ decay rapidly [$\dot{a}_{1,2} \sim O(F'(a_{ss}))$] towards their pseudo steady-state values in Eq. (3) for small deviations from a_{ss} . Under these conditions, the dynamical system in Eqs. (1)–(2) exhibit slow-fast dynamics in which after a short time [of order $1/F'(a_{ss})$], i.e., the fast part of the dynamics, the effects of initial conditions

of the amplitudes $a_{1,2}(0)$ are attenuated to zero, and the amplitudes track the phase difference adiabatically as described in Eq. (3), which is the slow part of the dynamics. It is important to note that Eqs. (3)–(4) represent the dynamics of Eqs. (1)–(2) accurately only in the slow part of the dynamics, where $t \gg 1/F'(a_{ss})$, and under the condition that there are two distinct time scales, $T_{\text{slow}} \sim O(1/\kappa)$ and $T_{\text{fast}} \sim O(1/F'(a_{ss}))$, where $F'(a_{ss}) \gg \kappa$. While the above assumptions limit the range of $\Delta\omega$, the phase model [Eq. (4)] is also valid when $|\Delta\omega| \gg \kappa$ and the phase difference runs freely $\dot{\psi} = \Delta\omega$, i.e., when the oscillators are effectively uncoupled.

Analysis

Inspection of Eq. (4) reveals that the phase difference dynamics can be mapped onto the noisy motion of an overdamped particle in a tilted washboard potential $V(\psi) = -\Delta\omega\psi - c_1\kappa \cos \psi - (c_2\kappa^2/2) \cos 2\psi$, see Methods. Furthermore, for small κ (weak coupling), Eq. (4) reduces to the well-known Adler equation^{6,22,23}. However, for non-small κ (non-weak coupling), the additional term $-c_2\kappa^2 \sin 2\psi$, can dramatically change the synchronization dynamics, including the birth of an additional pair of synchronized states (i.e., four extrema in V in each 2π interval) and enhanced synchronization range relative to the range of the Adler equation (Methods). We note that under the experimental conditions that we considered [$U_\infty = 8$ m/s, and $\ell_s = 0.4$ m], where $\kappa = 0.314$, $c_1 = 0.036$, and $c_2 = 0.043$, we only obtained an enhanced synchronization range (Supplementary Fig. 1). Moreover, by carrying the perturbation analysis to cubic order in κ , we find that the cubic order correction contains the additional terms $-c_3\kappa^3 \sin^3 \psi + r_1\zeta_1(t) + r_2\zeta_2(t)$; see Methods for details. Thus, the higher-order phase model in Eq. (4) is valid only when $c_2 \gg \kappa c_3$ and $|\zeta_3| \gg |r_{1,2}\zeta_{1,2}|$.

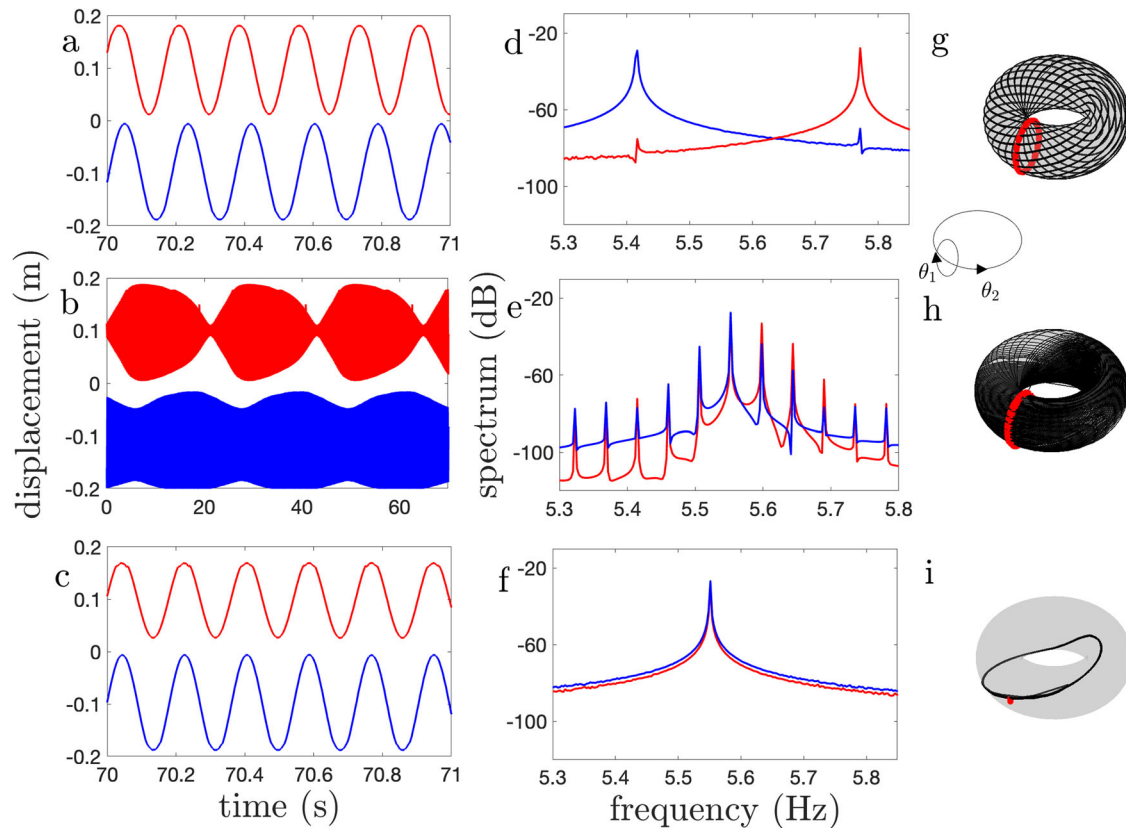


Fig. 3 | Analysis of the oscillators' motions. The experimentally measured displacements of the oscillators are shown in the time domain (a–c), frequency domain (d–f), toroidal phase space $\theta_{1,2} = \omega_{1,2}t + \phi_{1,2}$ and its respective Poincaré map $\theta_{1p}(k) = \theta_1(t_k)$, $\theta_{2p}(k) = \theta_2(t_k) = 2\pi k$ (g–i). For large frequency mismatch (dashed line in Fig. 2), the coupling effect is negligible, and oscillators run freely (a, d, g) with a small mutual injection of motion that can only be detected in the power spectra on dB scales. For moderate frequency mismatch (dotted line in Fig. 2), the coupling-

induced injected motion pulls the oscillators (b, e, h) toward synchronization. This injection pulling is highly visible both in time (beating envelopes) and frequency (side-bands with a spacing of the beats frequency) domains. For small frequency mismatch (dashed-dotted line in Fig. 2), the oscillators synchronized (c, f, i). The phase-locked synchronized motion is readily identified in the time and frequency domains, and associated with a unique trajectory in the toroidal phase space and a single fixed point in the Poincaré map.

The current of the phase difference $\langle \dot{\psi} \rangle = \lim_{t \rightarrow \infty} \langle \psi \rangle / t$ can be computed from the following expression⁴⁵

$$\langle \dot{\psi} \rangle = \frac{2\pi\sigma_3^2 (1 - e^{-2\pi\Delta\omega/\sigma_3^2})}{\int_0^{2\pi} \int_{\psi-2\pi}^{\psi} e^{-[V(\varphi)-V(\psi)]/\sigma_3^2} d\varphi d\psi}, \quad (5)$$

which we estimate numerically (Supplementary Note 2). In Fig. 2, we show the theoretical predictions of the normalized averaged amplitudes $\langle a_{1,2} \rangle / a_{ss}$ and the current $\langle \dot{\psi} \rangle$ from Eq. (3) and Eq. (5), along with the predictions from the Adler equation⁴⁶, and experimental data. The predictions of the Adler equation fail to describe the amplitude dependency on the frequency mismatch and the synchronization range (the predicted range is almost 20% shorter), while the higher-order model of Eq. (4) gives accurate predictions for the experiments.

To analyze the motion of the oscillators and distinguish between synchronized state (zero current $\langle \dot{\psi} \rangle \approx 0$), free-running state (non-zero current $\langle \dot{\psi} \rangle \neq 0$), and injection pulling, which is a transition state between free-running and synchronized states, we represent the measured signals in several domains. In Fig. 3, we show three samples from the experimental data of these three distinct states. The representations of the oscillators' signals in the time (panels a–c) and frequency (panels d–f) domains show distinctively different patterns that are readily identified with the different states of the oscillators. Furthermore, the construction of a torus from the total measured phases of the oscillators and a Poincaré map (panels g–i) reveals that unlike the dense toroidal phase space and Poincaré map of the free-running oscillators and injection pulling, in the synchronized state, the phase space and Poincaré map are sparse (signal trajectory and single fixed point).

Conclusions

Our demonstration of synchronizing two non-weakly coupled aeroelastic oscillators shows excellent agreement with analytical and numerical predictions. We experimentally control not only the frequency mismatch but also the coupling strength, which is essential for a complete description of the non-weakly coupled synchronized oscillators. The relatively simple macroscale mechanical system we used is easily characterized and tuned to operate at the desired conditions of a weakly nonlinear dynamical system with non-weak coupling (see Methods). Our results highlight the importance of non-weak coupling for enhanced synchronization range, which can be highly beneficial for various applications ranging from wireless communications⁴⁷ and time-keeping²⁴ to quantum networks⁴⁸. Our results extend the synchronization problem beyond weak coupling, relaxing the strict weak coupling requirement. This is achieved by replacing the Adler equation with a higher-order phase model that successfully describes the synchronization of two oscillators across a broad range of coupling strengths.

Methods

Measurements and characterization

To measure the transverse motions of the prisms, we marked each prism with duct tape, which appeared as a distinct rectangle region in the images, and we tracked its centroid to obtain the position of the prism as a function of time. We converted the pixel measurements to meters using a conversion meters-per-pixel (MPP) equation, which accurately accounts for the change in the length of the cantilevers. We calculated the MPP ratio by measuring the pixels at different lengths and utilizing the known width of the prisms. We then applied a trend line, resulting in the equation that converts the number of pixels to the displacement of each prism (see Supplementary Fig. 2). This process enabled a clear representation of the motions of the prisms, which was subsequently ready for analysis.

We estimated the linear, quadratic, and cubic damping coefficients in Supplementary Table 1 by analyzing the mechanical resonators' ring-down responses^{49,50}. We partitioned the decaying envelope of the signal into three amplitude regions (low, moderate, and high) and used the same technique of ref. 44 to estimate $\Gamma_{1,2,3}$. Using the estimated damping coefficient $\Gamma_{1,2,3}$, the

calculated resonators' properties $\omega_{1,2}$, m_r , η (Supplementary Table 1), and coefficients of the aerodynamic force ν_m, μ_n (based on the Parkinson model⁵¹, Supplementary Table 2, we constructed a theoretical amplitude response curve. We validated it with experimental measurements for several cantilever lengths (Fig. 4a). These validated response curves include multiple coexisting limit cycles (which we measured by sweeping the wind speed up and down) and variability of the limit-cycle amplitude as a function of the cantilevers' length. Therefore, we pick a wind speed of 8 m/s as the desired operating point at which the amplitudes of the various oscillators are relatively close to one another (less than 8% difference), and there are no multiple coexisting limit cycles. At this wind speed, we measure the steady-state power spectrum of the oscillator around its carrier frequency $f - f_{osc}$ and use a Lorentzian fit to extract the phase diffusion D (Fig. 4b). We note that the Lorentzian distribution only describes pure phase diffusion (i.e., negligible amplitude fluctuations)⁵², and the collapse of all experimental curves on the same Lorentzian distribution indicates a constant intensity of turbulence-induced random fluctuations (or, alternatively, that the delta-correlated Gaussian noise representation of the turbulence-induced random fluctuations in the amplitudes and phase equations is appropriate). More-

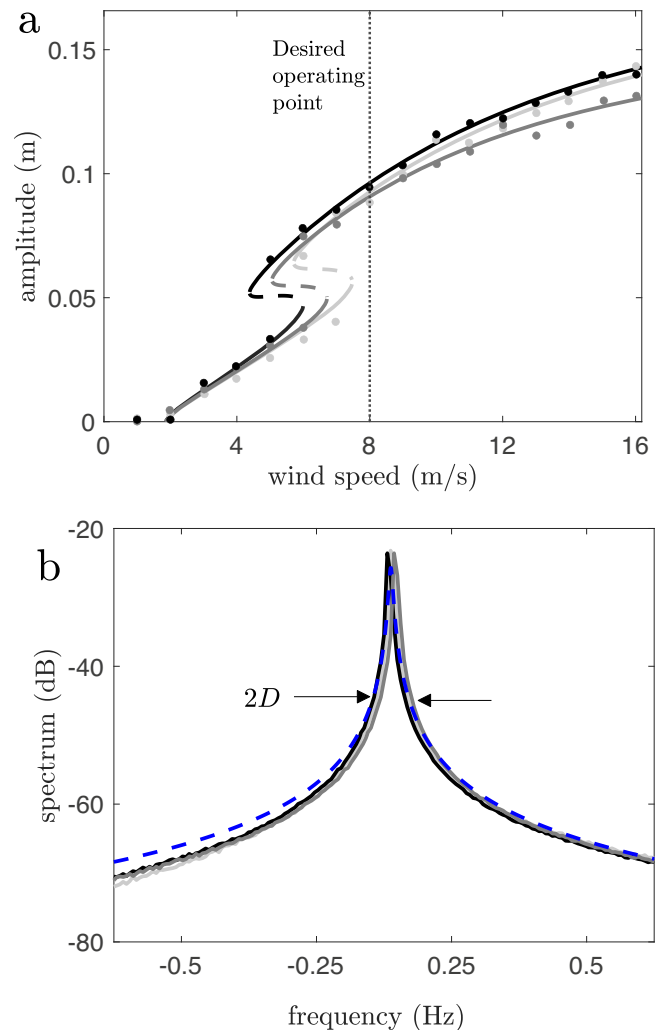


Fig. 4 | Steady-state response of a single aeroelastic oscillator. Experimental measurements of a single aeroelastic oscillator with various cantilever lengths (measured in meters): 0.62 (black), 0.59 (light gray), 0.56 (dark gray). The amplitude response curves exhibit a region of multiple coexisting limit cycles (stable/unstable denoted by solid/dashed curve) and non-identical responses for different cantilever lengths (a). The spectrum of the aeroelastic oscillator around its carrier frequency is almost identical regardless of the cantilevers' lengths (b) and closely follows the Lorentzian distribution (dashed blue curve).

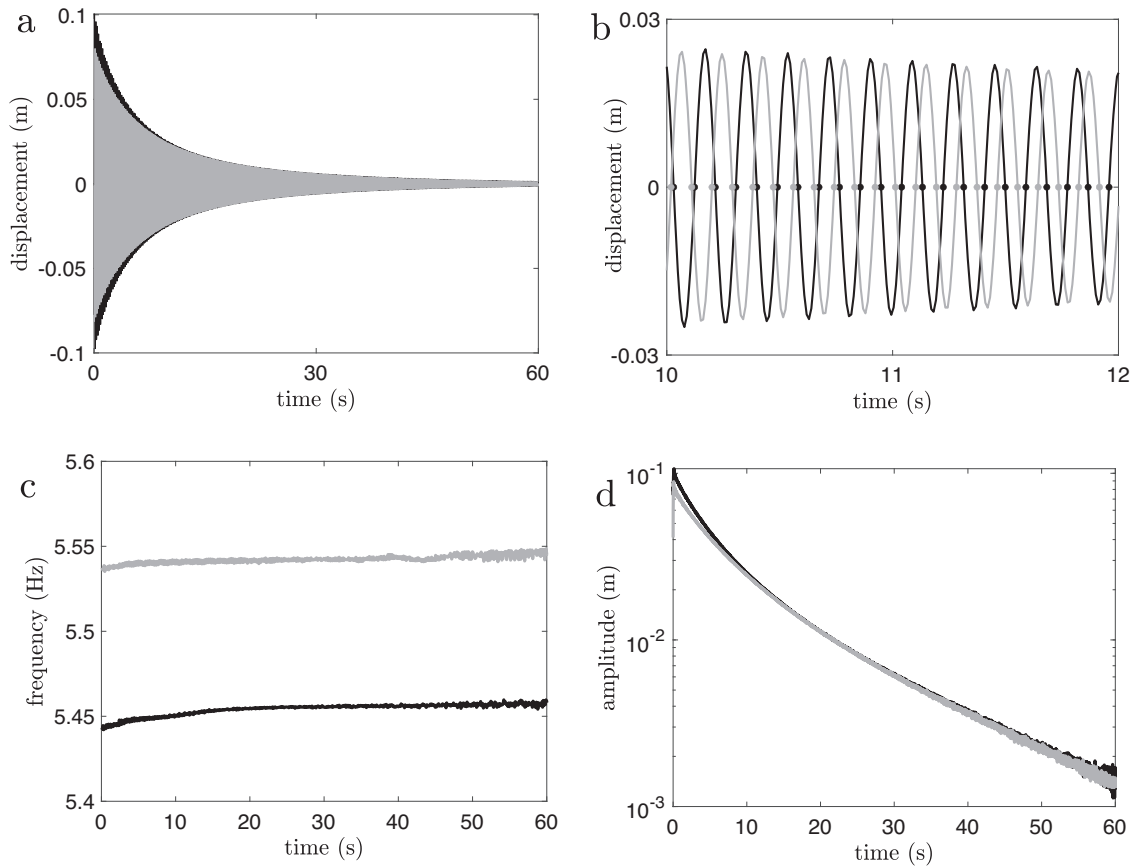


Fig. 5 | The ring down response. Estimation of coupling from the ring down response for $\ell = 0.59$ m and $\ell_s = 0.25$ m. By measuring the ring-down response (a) with/without (gray/black signals) coupling, we detect the zero-crossing of the signals

(b) and estimate the frequency (c) and amplitude (d) as functions of time. We estimate the reactive and dissipative coupling coefficients from the difference in frequency and amplitude.

over, the noise intensity in Eq. (2) is proportional to the measured phase diffusion $\sigma_3^2 = 2D/\omega_s = 5.23 \times 10^{-3}$.

For the coupling coefficients estimations (Supplementary Table 3), we perturbed each mechanical resonator from its equilibrium position in still air while holding the second resonator in its equilibrium position. By comparing the free oscillations decay toward the equilibrium position with and without coupling (Fig. 5a, b), we were able to extract the coupling-induced stiffness and damping. In particular, from the frequency shift $\Delta f = f_{\text{coupled}} - f_{\text{uncoupled}}$, we extracted the coupling stiffness $\Delta f = \omega_s \kappa / (2\pi)$, and from the slope of the decaying amplitude (at the linear decay regime), we extracted the coupling damping coefficient $\chi = d \ln[a_{\text{coupled}}(t)/a_{\text{uncoupled}}(t)]/dt$, where $\chi = \phi^2(\ell_s/\ell) c_{\text{cp}}/[\rho \ell(1 + 2\mu)]$. We note that Δf remained approximately constant (Fig. 5c) during the ring-down experiments for the various set-ups we considered, and hence, we deduce that the reactive coupling is linear. The difference in the decaying amplitude in the presence and absence of coupling is relatively small (Fig. 5d), and we could only measure a slight difference in the linear decay, which revealed that $\kappa \gg \chi/\omega_s$, and hence, that the dissipative coupling is negligible with respect to the reactive coupling.

Higher-order phase model

As described in subsection II B, we use a standard perturbation method to obtain the higher-order phase model. That is, we calculate the small perturbations of the expansion $a_{1,2} = a_{ss} + \sum_n \kappa^n \delta a_{1,2}^{(n)}$ by substituting the expansion into Eq. (1) and equating terms of equal powers of κ to get the following set of equations

$$O(1) : F(a_{ss}) = 0, \tag{6}$$

$$O(\kappa) : \delta \dot{a}_{1,2}^{(1)} = -F'(a_{ss}) \delta a_{1,2}^{(1)} \pm a_{ss} \sin \psi, \tag{7}$$

$$O(\kappa^2) : \delta \dot{a}_{1,2}^{(2)} = -F'(a_{ss}) \delta a_{1,2}^{(2)} \pm \delta a_{2,1}^{(1)} \sin \psi - \frac{1}{2} (\delta a_{1,2}^{(1)})^2 F''(a_{ss}), \tag{8}$$

$$O(\kappa^3) : \delta \dot{a}_{1,2}^{(3)} = -F'(a_{ss}) \delta a_{1,2}^{(3)} \pm \delta a_{2,1}^{(2)} \sin \psi - \delta a_{1,2}^{(1)} \delta a_{1,2}^{(2)} F''(a_{ss}) - \frac{1}{6} (\delta a_{1,2}^{(1)})^3 F'''(a_{ss}) + \zeta_{1,2}^{(\text{rs})}(t), \tag{9}$$

where $\zeta_{1,2}(t) = \kappa^2 \zeta_{1,2}^{(\text{rs})}(t)$. The zero-order equation, Eq. (6), is the steady-state equation of the uncoupled oscillators, which is satisfied immediately. We see that the perturbations $\delta a_{1,2}^{(n)}$ of the steady-state amplitude a_{ss} are strongly damped [$F'(a_{ss})$ is the effective damping constant], and so, for $t \gg 1/F'(a_{ss})$, we can assume $\delta \dot{a}_{1,2}^{(n)} \approx 0$ (see Appendix B of ref. 53 for detailed proof). Thus, from the first-order equation, Eq. (7), we find that $\delta a_{1,2}^{(1)} = \pm a_{ss} \sin \psi / F'(a_{ss})$, which we substitute into Eq. (8) to obtain $\delta a_{1,2}^{(2)} = -a_{ss} [2F'(a_{ss}) + a_{ss} F''(a_{ss})] \sin^2 \psi / [2F'^3(a_{ss})]$. Finally, we substitute $\delta a_{1,2}^{(1)}$ and $\delta a_{1,2}^{(2)}$ into Eq. (9) to find that $\delta a_{1,2}^{(3)} = \zeta_{1,2}^{(\text{rs})}(t) / F'(a_{ss}) \mp a_{ss} \{6F'^2(a_{ss}) - 3a_{ss}^2 F''^2(a_{ss}) + a_{ss} F'(a_{ss}) [a_{ss} F'''(a_{ss}) - 3F''(a_{ss})]\} \sin^3 \psi / [6F'^5(a_{ss})]$. By substituting the expansion of the amplitudes into Eq. (2), we find that

$$\begin{aligned} \dot{\psi} = & \Delta\omega - c_1 \kappa \sin \psi - c_2 \kappa^2 \sin 2\psi - c_3 \kappa^3 \sin^3 \psi \\ & + r_1 \zeta_1(t) + r_2 \zeta_2(t) + \zeta_3(t), \end{aligned} \tag{10}$$

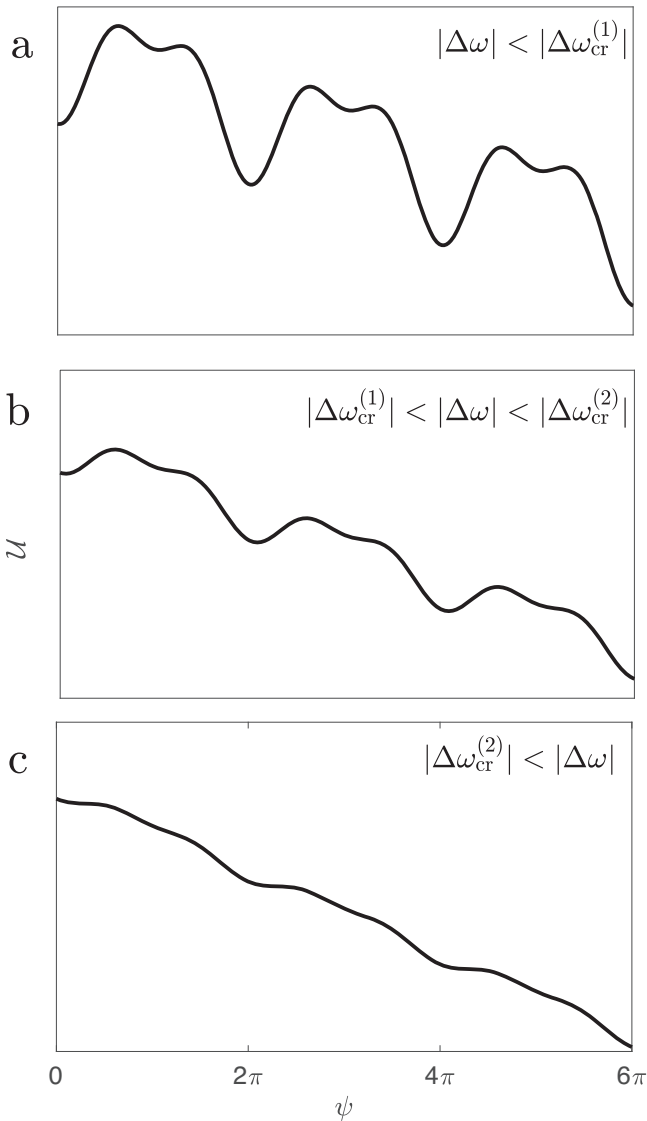


Fig. 6 | Extrema of the washboard potential. The local extrema of $V(\psi)$ [Eq. (12)] in each 2π interval corresponds to synchronized states, where local minima are stable states, and local maxima are unstable states. If $d > 0$, then for small values of $\Delta\omega$, there are two pairs of stable and unstable synchronized states (a); for moderate values of $\Delta\omega$, there is a single pair of stable and unstable synchronized states (b), and there are no synchronized states for large values of $\Delta\omega$ (c).

where

$$r_{1,2} = \frac{(\partial_{a_{1,2}} G)|_{a_{ss}}}{F'(a_{ss})}, \quad c_1 = \frac{a_{ss}}{F'(a_{ss})} (\partial_{a_2} G - \partial_{a_1} G)|_{a_{ss}},$$

$$c_2 = \frac{2}{F'(a_{ss})}, \quad c_3 = \frac{a_{ss}}{6F'^3(a_{ss})} \left\{ 3a_{ss}^2 F''^2(a_{ss}) [\partial_{a_2} G - \partial_{a_1} G]_{a_{ss}} \right.$$

$$+ a_{ss} F'(a_{ss}) \left[a_{ss} F'''(a_{ss}) (\partial_{a_1} G - \partial_{a_2} G)|_{a_{ss}} \right.$$

$$+ 3F''(a_{ss}) (\partial_{a_2} G - \partial_{a_1} G - a_{ss} \partial_{a_2}^2 G + a_{ss} \partial_{a_1}^2 G)|_{a_{ss}} \left. \right]$$

$$+ F'^2(a_{ss}) \left[6(\partial_{a_1} G - \partial_{a_2} G)|_{a_{ss}} \right.$$

$$\left. + a_{ss} (6\partial_{a_1}^2 G - 6\partial_{a_2}^2 G - a_{ss} \partial_{a_1}^3 G + a_{ss} \partial_{a_2}^3 G)|_{a_{ss}} \right] \left. \right\}.$$

Thus, when $c_2 \gg \kappa c_3$ and $|\zeta_3| \gg |r_{1,2} \zeta_{1,2}|$, Eq (10) reduces to Eq. (4), i.e., to the higher-order phase model that we analyze in this paper.

Eq. (4) can be written compactly as

$$\dot{\psi} = -\frac{dV}{d\psi} + \zeta_3(t), \tag{11}$$

where

$$V(\psi) = -\Delta\omega\psi - c_1 \kappa \cos \psi - \frac{c_2 \kappa^2}{2} \cos 2\psi \tag{12}$$

is an effective washboard potential, and its local minima correspond to stable synchronized states. From Eq. (12), we find that if the condition $d = 16c_2^2 \kappa^2 - c_1(\sqrt{32c_2^2 \kappa^2 + c_1^2} + c_1) > 0$ is satisfied, then the potential $V(\psi)$ has in each 2π interval: two pairs of stable and unstable synchronized states when $|\Delta\omega| < |\Delta\omega_{cr}^{(1)}|$ (Fig. 6a), a single pair of stable and unstable synchronized states when $|\Delta\omega_{cr}^{(1)}| < |\Delta\omega| < |\Delta\omega_{cr}^{(2)}|$ (Fig. 6b), and no synchronized states when $|\Delta\omega_{cr}^{(2)}| < |\Delta\omega|$ (Fig. 6c). The critical values of the frequency mismatch $\Delta\omega_{cr}^{(1,2)}$ in which saddle-node bifurcations occur, are given by

$$\Delta\omega_{cr}^{(1,2)} < \frac{(\sqrt{32c_2^2 \kappa^2 + c_1^2} \mp 3c_1)}{16\sqrt{2}c_2} \times \sqrt{16c_2^2 \kappa^2 \mp c_1 (\sqrt{32c_2^2 \kappa^2 + c_1^2} \pm c_1)}. \tag{13}$$

If the condition $d > 0$ is not satisfied (as in our experiments, where $d < 0$), then we can have, at most (when $|\Delta\omega| < |\Delta\omega_{cr}^{(2)}|$), a single pair of stable and unstable synchronized states.

Data availability

The data supporting this study’s findings are available from the corresponding author upon reasonable request.

Received: 15 February 2024; Accepted: 20 June 2024;

Published online: 29 June 2024

References

1. Van Duzer, T. & Turner, C. *Principles of Superconductive Devices and Circuits* (Elsevier, 1981).
2. Anderson, P. W. Considerations on the flow of superfluid helium. *Rev. Mod. Phys.* **38**, 298 (1966).
3. Strogatz, S. H. *Sync: How Order Emerges from Chaos in the Universe, Nature, and Daily Life* (Hachette UK, 2012).
4. Kuramoto, Y. *Chemical Oscillations, Waves, and Turbulence*, vol. 19 (Springer Science & Business Media, 2012).
5. Kuramoto, Y. & Nakao, H. On the concept of dynamical reduction: the case of coupled oscillators. *Philos. Trans. R. Soc. A* **377**, 20190041 (2019).
6. Pikovsky, A., Rosenblum, M., Kurths, J. & Kurths, J. *Synchronization: A Universal Concept In Nonlinear Sciences*, vol. 12 (Cambridge University Press, 2003).
7. León, I. & Nakao, H. Analytical phase reduction for weakly nonlinear oscillators. *Chaos Solitons Fractals* **176**, 114117 (2023).
8. Martens, E. A. et al. Integrability of a globally coupled complex Riccati array: Quadratic integrate-and-fire neurons, phase oscillators, and all in between. *Phys. Rev. Lett.* **132**, 057201 (2024).
9. Pecora, L. M., Sorrentino, F., Hagerstrom, A. M., Murphy, T. E. & Roy, R. Cluster synchronization and isolated desynchronization in complex networks with symmetries. *Nat. Commun.* **5**, 4079 (2014).
10. Popovych, O. V., Maistrenko, Y. L. & Tass, P. A. Phase chaos in coupled oscillators. *Phys. Rev. E* **71**, 065201 (2005).

11. Wolfrum, M., Gurevich, S. V. & Omel'chenko, O. E. Turbulence in the Ott–Antonsen equation for arrays of coupled phase oscillators. *Nonlinearity* **29**, 257 (2016).
12. Duguet, Y. & Maistrenko, Y. L. Loss of coherence among coupled oscillators: from defect states to phase turbulence. *Chaos: an interdisciplinary journal of nonlinear science* **29**, 121103 (AIP Publishing, 2019).
13. Abrams, D. M. & Strogatz, S. H. Chimera states for coupled oscillators. *Phys. Rev. Lett.* **93**, 174102 (2004).
14. Martens, E. A., Laing, C. R. & Strogatz, S. H. Solvable model of spiral wave chimeras. *Phys. Rev. Lett.* **104**, 044101 (2010).
15. Martens, E. A., Thutupalli, S., Fourrière, A. & Hallatschek, O. Chimera states in mechanical oscillator networks. *Proc. Natl. Acad. Sci.* **110**, 10563–10567 (2013).
16. Matheny, M. H. et al. Exotic states in a simple network of nanoelectromechanical oscillators. *Science* **363**, eaav7932 (2019).
17. Taira, K. & Nakao, H. Phase-response analysis of synchronization for periodic flows. *J. Fluid Mech.* **846**, R2 (2018).
18. Khodkar, M. A. & Taira, K. Phase-synchronization properties of laminar cylinder wake for periodic external forcings. *J. Fluid Mech.* **904**, R1 (2020).
19. Um, E. et al. Phase synchronization of fluid-fluid interfaces as hydrodynamically coupled oscillators. *Nat. Commun.* **11**, 5221 (2020).
20. Godavarthi, V., Kawamura, Y. & Taira, K. Optimal waveform for fast synchronization of airfoil wakes. *J. Fluid Mech.* **976**, R1 (2023).
21. Cross, M. Improving the frequency precision of oscillators by synchronization. *Phys. Rev. E* **85**, 046214 (2012).
22. Agrawal, D. K., Woodhouse, J. & Seshia, A. A. Observation of locked phase dynamics and enhanced frequency stability in synchronized micromechanical oscillators. *Phys. Rev. Lett.* **111**, 084101 (2013).
23. Matheny, M. H. et al. Phase synchronization of two anharmonic nanomechanical oscillators. *Phys. Rev. Lett.* **112**, 014101 (2014).
24. Zhang, M., Shah, S., Cardenas, J. & Lipson, M. Synchronization and phase noise reduction in micromechanical oscillator arrays coupled through light. *Phys. Rev. Lett.* **115**, 163902 (2015).
25. Jang, J. K. et al. Synchronization of coupled optical microresonators. *Nat. Photonics* **12**, 688–693 (2018).
26. Kim, B. Y. et al. Synchronization of nonsolitonic Kerr combs. *Sci. Adv.* **7**, eabi4362 (2021).
27. Rodrigues, C. C. et al. Optomechanical synchronization across multi-octave frequency spans. *Nat. Commun.* **12**, 5625 (2021).
28. Zahedinejad, M. et al. Two-dimensional mutually synchronized spin hall nano-oscillator arrays for neuromorphic computing. *Nat. Nanotechnol.* **15**, 47–52 (2020).
29. Zahedinejad, M. et al. Memristive control of mutual spin hall nano-oscillator synchronization for neuromorphic computing. *Nat. Mater.* **21**, 81–87 (2022).
30. Marković, D. Synchronization by memristors. *Nat. Mater.* **21**, 4–5 (2022).
31. Kurebayashi, W., Shirasaka, S. & Nakao, H. Phase reduction method for strongly perturbed limit cycle oscillators. *Phys. Rev. Lett.* **111**, 214101 (2013).
32. Wilson, D. & Ermentrout, B. Phase models beyond weak coupling. *Phys. Rev. Lett.* **123**, 164101 (2019).
33. Wilson, D. & Ermentrout, B. Augmented phase reduction of (not so) weakly perturbed coupled oscillators. *SIAM Rev.* **61**, 277–315 (2019).
34. Gengel, E., Teichmann, E., Rosenblum, M. & Pikovsky, A. High-order phase reduction for coupled oscillators. *J. Phys.: Complex.* **2**, 015005 (2020).
35. Mau, E. T., Rosenblum, M. & Pikovsky, A. High-order phase reduction for coupled 2d oscillators. *Chaos: an interdisciplinary journal of nonlinear science* **33**, 101101 (AIP Publishing, 2023).
36. Adler, R. A study of locking phenomena in oscillators. *Proc. IRE* **34**, 351–357 (1946).
37. Pérez-Cervera, A. et al. Global phase-amplitude description of oscillatory dynamics via the parameterization method. *Chaos: an interdisciplinary journal of nonlinear science* **30**, 083117 (AIP Publishing, 2020).
38. Kurebayashi, W., Yamamoto, T., Shirasaka, S. & Nakao, H. Phase reduction of strongly coupled limit-cycle oscillators. *Phys. Rev. Res.* **4**, 043176 (2022).
39. Bick, C., Böhle, T. & Kuehn, C. Higher-order network interactions through phase reduction for oscillators with phase-dependent amplitude. *arXiv preprint arXiv:2305.04277* (2023).
40. von der Gracht, S., Nijholt, E. & Rink, B. A parametrisation method for high-order phase reduction in coupled oscillator networks. *arXiv preprint arXiv:2306.03320* (2023).
41. Haken, H., Kelso, J. S. & Bunz, H. A theoretical model of phase transitions in human hand movements. *Biol. Cybern.* **51**, 347–356 (1985).
42. Haken, H. *Synergetics: Introduction and Advanced Topics*. Physics and astronomy online library (Springer, 2004).
43. Shoshani, O. Theoretical aspects of transverse galloping. *Nonlinear Dyn.* **94**, 2685–2696 (2018).
44. Regev, S. & Shoshani, O. Investigation of transverse galloping in the presence of structural nonlinearities: theory and experiment. *Nonlinear Dyn.* **102**, 1197–1207 (2020).
45. Reimann, P. et al. Giant acceleration of free diffusion by use of tilted periodic potentials. *Phys. Rev. Lett.* **87**, 010602 (2001).
46. Stratonovich, R. L. *Topics in the Theory of Random Noise* Vol. 2 (CRC Press, 1967).
47. Kaka, S. et al. Mutual phase-locking of microwave spin torque nano-oscillators. *Nature* **437**, 389–392 (2005).
48. Laskar, A. W. et al. Observation of quantum phase synchronization in spin-1 atoms. *Phys. Rev. Lett.* **125**, 013601 (2020).
49. Polunin, P. et al. Characterizing mems nonlinearities directly: The ring-down measurements. In *Solid-State Sensors, Actuators and Microsystems (TRANSDUCERS), 2015 Transducers-2015 18th International Conference on*, 2176–2179 (IEEE, 2015).
50. Polunin, P. M., Yang, Y., Dykman, M. I., Kenny, T. W. & Shaw, S. W. Characterization of mems resonator nonlinearities using the ringdown response. *J. Microelectromech. Syst.* **25**, 297–303 (2016).
51. Parkinson, G. & Smith, J. The square prism as an aeroelastic nonlinear oscillator. *Q. J. Mech. Appl. Math.* **17**, 225–239 (1964).
52. Rubiola, E. *Phase Noise and Frequency Stability in Oscillators* (Cambridge University Press, 2008).
53. Shoshani, O. & Shaw, S. W. Phase noise reduction and optimal operating conditions for a pair of synchronized oscillators. *IEEE Trans. Circuits Syst. I Regul. Pap.* **63**, 1–11 (2016).

Acknowledgements

This work is supported by ISF under grant number 344/22. OS is also partially supported by the Pearlstone Center for Aeronautical Engineering Studies at BGU.

Author contributions

D.S.F. and O.S. conceived the idea. D.S.F. collected the data and performed the experiments. O.S. formulated the theoretical modeling. D.S.F. conducted analytical and numerical analysis and performed the fitting with the experimental data. D.S.F. and O.S. designed the experiments. The project was supervised by O.S. Both authors contributed to the data analysis, interpretation of the results, and writing of the manuscript, with the main contribution from O.S.

Competing interests

The authors declare no competing interests.

Additional information

Supplementary information The online version contains supplementary material available at <https://doi.org/10.1038/s42005-024-01706-6>.

Correspondence and requests for materials should be addressed to Oriel Shoshani.

Peer review information *Communications Physics* thanks Sho Shirasaka and the other, anonymous, reviewer(s) for their contribution to the peer review of this work. A peer review file is available.

Reprints and permissions information is available at <http://www.nature.com/reprints>

Publisher's note Springer Nature remains neutral with regard to jurisdictional claims in published maps and institutional affiliations.

Open Access This article is licensed under a Creative Commons Attribution 4.0 International License, which permits use, sharing, adaptation, distribution and reproduction in any medium or format, as long as you give appropriate credit to the original author(s) and the source, provide a link to the Creative Commons licence, and indicate if changes were made. The images or other third party material in this article are included in the article's Creative Commons licence, unless indicated otherwise in a credit line to the material. If material is not included in the article's Creative Commons licence and your intended use is not permitted by statutory regulation or exceeds the permitted use, you will need to obtain permission directly from the copyright holder. To view a copy of this licence, visit <http://creativecommons.org/licenses/by/4.0/>.

© The Author(s) 2024